

Low-energy negative muon interaction with matter

Petar Danev^{a,*}, Andrzej Adamczak^b, Dimitar Bakalov^a, Emiliano Mocchiutti^c, Mihail Stoilov^a, and Andrea Vacchi^{d,c}

^a*Institute for Nuclear Research and Nuclear Energy, Bulgarian Academy of Sciences,
blvd. Tsarigradsko ch. 72, Sofia 1142, Bulgaria*

E-mail: petar_danev@abv.bg

^b*Institute of Nuclear Physics, Polish Academy of Sciences,
Radzikowskiego 152, PL31342 Kraków, Poland*

^c*Istituto Nazionale di Fisica Nucleare,
Padriciano 99, AREA Science Park, 34149 Trieste, Italy*

^d*Mathematics and Informatics Department, Udine University
via delle Scienze 206, Udine*

ABSTRACT: The interaction of negatively charged muons with solid material layers of aluminum, gold, stainless steel, polystyrene and gaseous hydrogen is studied by Monte Carlo methods. Empirical expressions for the functional dependence of the final muon momentum and spatial distribution on the parameters of the media and on initial muon momenta up to 75 MeV/c are derived. These results help restrict to a narrower range the search for optimal parameters in full scale MC simulations of experiments with light gas muonic atoms.

KEYWORDS: Detector modelling and simulations; Particle tracking detectors; Simulation methods and programs.

*Corresponding author.

Contents

1. Introduction	1
2. Propagation of negative muons across solid material layers	2
2.1 Muon survival probability	3
2.2 Momentum and angular composition of the scattered muon beam	4
3. Stopping negative muons in gaseous hydrogen	7
4. Discussion of the results	9

1. Introduction

The laser spectroscopy measurement of the hyperfine splitting in the ground state of muonic hydrogen, considered as fundamental test of QED, complementary to the measurement in ordinary hydrogen [1], has been a major experimental challenge for more than two decades [2, 3]. The interest in it grew up significantly when the muonic hydrogen Lamb shift experiment revealed a 9σ discrepancy between the proton charge radius values extracted from muonic hydrogen spectroscopy and $e - p$ scattering data [4]. The point was that from the hyperfine splitting of muonic hydrogen one can directly extract the value of the Zemach radius of the proton [5], juxtapose it to the value extracted from ordinary hydrogen spectroscopy [6] and this way test most of the hypotheses put forward to explain the proton size puzzle. The FAMU collaboration [7] is currently preparing an experiment that uses a method based on the study of the diffusion of the hydrogen muonic atoms in appropriate gas target and its response to monochromatic laser radiation of resonance frequency [8, 9]. An alternative experimental approach has been recently suggested in [10].

As discussed in details in [3, 8, 9], the efficiency of the method adopted by the FAMU team is determined by the energy dependence in the epithermal range of the rate of muon transfer in collisions of the muonic hydrogen atoms with the atoms of the heavier gas admixture. There are experimental indications that muon transfer to oxygen has the needed characteristics [11], in agreement with the theoretical estimates [12, 13], but the experimental accuracy is far from being sufficient for planning and optimizing the measurement of the hyperfine splitting. Because of this, an experiment uniquely dedicated to the thorough investigation of the collision energy dependence of the rate of muon transfer to various gases was launched as a preliminary stage of the FAMU project. The measurements will be performed at the pulsed muon source of the RAL-RIKEN facility [14]. Muons of initial momentum in the 50-70 MeV/c range will be stopped in a mixture of hydrogen and various heavier gases at high pressure, and the time distribution of the characteristic X-rays signalling the transfer of the muon to the admixture nuclei will be registered and analyzed using the algorithms of [9].

One of the main challenges in the preparation of the experimental set-up was the design of the gas target which was supposed to fulfill the following conditions:

1. as much as possible of the incident muons are stopped in gas, i.e. the losses in the front, side and rear walls of the gas container are minimized;
2. as large part as possible of the emitted characteristic X-rays reach the radiation detectors around the gas target that, in principle, cover only a small fraction of the solid angle ;
3. the background, mainly due to the electrons produced in muon decay, is suppressed as strongly as possible.

Cond. 1 requires the detailed study of the balance between the stopping power of the gas as function of the muon momentum and the pressure (with account of the dependence of the muon flux on the initial momentum), and the losses in the front wall that depend on its composition and thickness. Cond. 2 requires the study of the spatial aspects of the diffusion and stopping of the muonic atoms. Finally, Cond. 3 needs the interaction of the muons with the container wall ingredients to be taken into account. During the search for the optimal target and detector set-up a large variety of geometrical configurations and materials were considered and investigated with Monte Carlo simulation codes. Leaving the detailed description of the selected experimental design to be reported elsewhere, we present here some characteristics and regularities of the propagation of negative muons in materials, established empirically with the FLUKA simulation code [15, 16], which we found particularly useful in the preliminary stages of the set-up design and, we believe, are applicable to a broad range of muon physics modelling problems.

We focused our attention on two “elemental” cases: (a) a monochromatic collinear muon beam normally incident on a solid homogeneous layer made out of some of the materials of interest (steel, aluminum, gold, and polystyrene), and (b) a monochromatic collinear muon beam stopped in an unbound domain filled with hydrogen. In case (a), only part $Q, Q \leq 1$ of the incident muons cross the layer; they are scattered at angle Θ with final momentum p' , in general different from the initial momentum p . We studied the probability distributions of p' and Θ as functions of p and the layer thickness d and derived simple approximate expressions for the mean and root mean squared (r.m.s.) deviation values, as well for the surviving rate Q . These expressions were verified to provide satisfactory accuracy for $p \leq 75$ MeV/c - the range of initial momenta available at the RAL-RIKEN facility. In case (b) the muons are slowed in collisions with the hydrogen molecules and then stopped and captured in muonic hydrogen atoms. We investigated the spatial distribution of the stopping points and derived simple approximate expressions for the mean value and root mean squared deviation of the cylindrical coordinates z and r of the stopping points as functions of the initial momentum p and the hydrogen gas pressure H . In principle, these formulae could be used to model the propagation and stopping of non-monochromatic muon beams in complex geometrical configurations, but undoubtedly such an approach will be much less efficient and accurate than the direct Monte Carlo simulations. The reported results were intended only as – and shown to be – a convenient tool for the preliminary estimation of the impact of individual elements during the process of designing complex set-ups for the experimental study of muonic atoms.

2. Propagation of negative muons across solid material layers

In this section we consider the interaction of negative muons with four materials of interest: Aluminum (denoted by **A**), stainless steel 316LN [17] (**S**), Gold (**G**), and Polystyrene (**P**) using sim-

ulated results obtained with the FLUKA code [15, 16]. In each run monochromatic bunches of $N = 10^5$ muons with initial momentum p , $15 \leq p \leq 75$ MeV/c are launched against a layer of material $\mathbf{M}=\mathbf{A}$, \mathbf{S} , \mathbf{G} or \mathbf{P} with thickness d along the z -axis, normal to the layer surface (see Figure 1a).

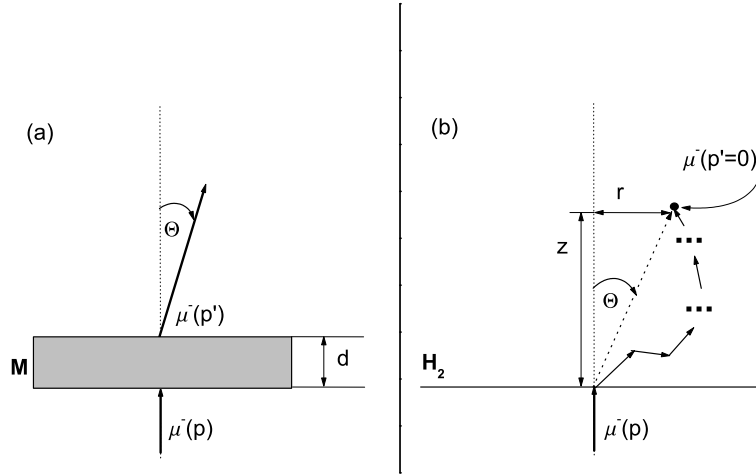


Figure 1. Geometry of the simulated events. (a) Muons with momentum p cross normally the boundary of a layer of material \mathbf{M} with thickness d . The momentum p' and the scattering angle Θ at the crossing with the opposite boundary are evaluated using the FLUKA code. (b) Muons with initial momentum p propagate in hydrogen medium at gas pressure H . The coordinates z , r , and Θ of the muon stopping points are evaluated with FLUKA.

2.1 Muon survival probability

Denote number of muons, stopped within the layer, by $N_0(p, d; \mathbf{M})$, $0 \leq N_0(p, d; \mathbf{M}) \leq N$. In terms of the latter the empirical probability distribution for a muon with initial momentum p to cross a layer of thickness d is $Q(p, d; \mathbf{M}) = 1 - N_0(p, d; \mathbf{M})/N$. Figure 2 shows “the rate of survival” $Q(p, d; \mathbf{A})$ of a monochromatic muon beam versus the initial momentum p , for a set of values of the Aluminum layer thickness d . For momenta below the breakdown thickness-dependent value $p_0(d; \mathbf{M})$ practically all the muons are stopped in the Al layer; for momenta above $p_0(d; \mathbf{M})$ practically all muons pass through the layer. The interval of p within which Q rises from $Q \sim 20\%$ to $Q \sim 80\%$ is as narrow as 1 MeV/c. We define the breakdown momentum by $Q(p_0(d; \mathbf{M}), d; \mathbf{M}) = 0.5$, evaluate $p_0(d; \mathbf{M})$ for a set of values of the thickness d between 0.01 mm and 8 mm and find out that the following 2-parameter expression fits very well the calculated values:

$$p_0(d; \mathbf{M}) = a_1 d^{a_2} \quad (2.1)$$

The values of the parameters a_1 and a_2 for the material of interest are given in Table 1.

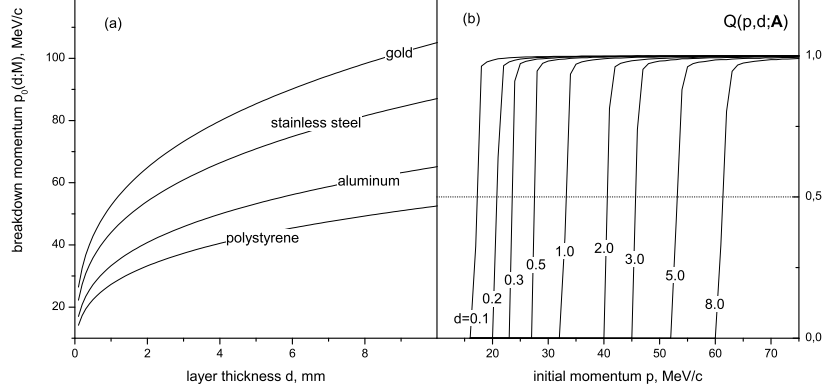


Figure 2. Interaction of a muon beam with solid material layers. (a) The breakdown momentum $p_0(d;M)$ versus the thickness d of the layer of material M . (b) Probability $Q(p,d;A)$ that a normally incident muon with initial momentum p is not stopped in aluminum layer of thickness $d, 0.1 \leq d \leq 8$ mm.

Table 1. Numerical values of the coefficients $a_i, i = 1, 2$ in the fitting expression for the breakdown momenta p_0 (2.1).

M	P	A	S	G
$a_1, \text{MeV/c}$	27.3	33.3	44.0	52.7
a_2	0.2842	0.2916	0.2964	0.2997
$\rho, \text{g cm}^{-3}$	1.03	2.7	7.99	19.29

It is worth mentioning that the values of the breakdown momentum p_0 , calculated with FLUKA for the four materials listed above, are quite accurately fitted with the single 3-parameter expression

$$p_0(d, \mathbf{M}) = a_1 d^{a_2} \rho_{\mathbf{M}}^{a_3}, \quad (2.2)$$

where $\rho_{\mathbf{M}}$ is the density of the material \mathbf{M} (in g cm^{-3} , see Table 1), d is the thickness (in mm), and $a_1 = 26.6 \text{ MeV/c}$, $a_2 = 0.2969$, and $a_3 = 0.2342$. Note, however, that Eq. (2.2) has not been verified for other materials.

2.2 Momentum and angular composition of the scattered muon beam

From the values of the final momentum p' and the scattering angle Θ , simulated with FLUKA for the $N_1 = N - N_0$ muons that cross the layer (see Figure 1) we evaluated the empirical probability densities $f(p'; d, p, \mathbf{M})$ and $f(\Theta; d, p, \mathbf{M})$ of the final momentum and angular distribution of the outgoing muons as functions of the initial momentum p , the thickness d and the material \mathbf{M} of the layer. Figure 3 illustrates the effects of aluminum layers with thickness $0.1 \leq d \leq 8$ mm on a monochromatic beam with $p = 60 \text{ MeV/c}$, incl. the slowing down and broadening of the momentum and angular profile for thicker layers. To make these results helpful for practical use, we evaluated and tabulated the mean values $\langle p' \rangle, \langle \Theta \rangle$ and the root mean square deviations $\sigma_{p'}, \sigma_{\Theta}$ of the final

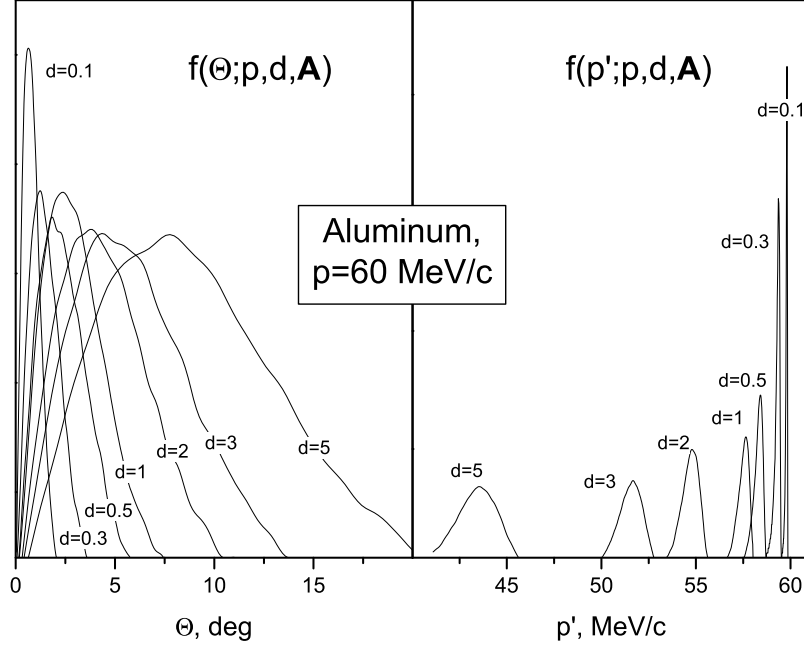


Figure 3. (a) Probability density of the distribution of the scattering angle Θ of the outgoing muons with initial momentum $p = 60$ MeV/c, at the crossing with the boundary of an aluminum layer of thickness d , in arbitrary units; (b) Same for the probability density of the distribution of the outgoing momentum p' .

momentum p' and the scattering angle Θ as functions of p and d . Figure 4 shows the curves for aluminum layer with thickness $0.1 \leq d \leq 8$ mm. Then, we fitted the table values with few-parameter analytical expression and obtained the following approximants:

$$\langle p' \rangle(p, d; \mathbf{M}) = c_1^{(1)} d(1 - d^2) + p(c_2^{(1)} d^2 + c_3^{(1)} d + 1) + \quad (2.3)$$

$$(c_4^{(1)} d^2 + c_5^{(1)} d + c_6^{(1)}) (d^6 \exp(-(p - 48)))^{(c_7^{(1)} + c_8^{(1)}/d)}$$

$$\sigma_{p'}(p, d; \mathbf{M}) = c_1^{(2)} \sqrt{d} + (c_2^{(2)} + c_3^{(2)} \sqrt{d}) / (p - c_4^{(2)} - c_5^{(2)} d c_6^{(2)}) \quad (2.4)$$

$$\langle \Theta \rangle(p, d; \mathbf{M}) = \left(\underbrace{\sum_{i=0}^3 \sum_{j=0}^2 c_{ij}^{(3)} d^i p^j + \bar{c}_1^{(3)} p^2 / d^2 + \bar{c}_2^{(3)} \sqrt{d} p^2 + \bar{c}_3^{(3)} d^3 / \sqrt{p}}_{i+j \leq 3} \right)^{-1} \quad (2.5)$$

$$\sigma_{\Theta}(p, d; \mathbf{M}) = \left(\underbrace{\sum_{i=0}^3 \sum_{j=0}^2 c_{ij}^{(4)} d^i p^j + \bar{c}_1^{(4)} p^2 / d^2 + \bar{c}_2^{(4)} \sqrt{d} p^2 + \bar{c}_3^{(4)} d^3 / \sqrt{p}}_{i+j \leq 3} \right)^{-1} \quad (2.6)$$

The numerical values of the parameters in these fitting formulae, calculated for the materials of interest $\mathbf{M}=\mathbf{P}$ (polystyrene), \mathbf{A} (aluminum), \mathbf{S} (stainless steel 316LN), and \mathbf{G} (gold), are given in

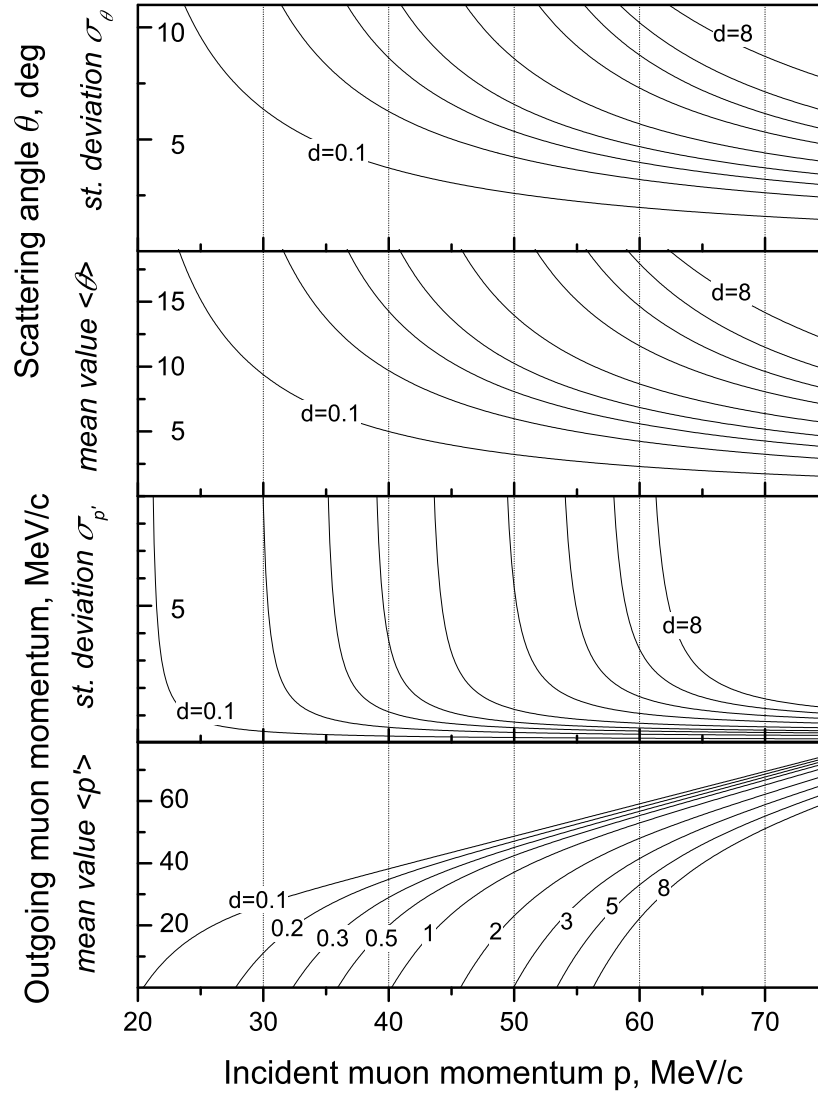


Figure 4. Momentum spectrum and angular profile of outgoing muon beams. Plotted are the mean values $\langle p' \rangle$, $\langle \Theta \rangle$ and the r.m.s. deviations $\sigma_{p'}$, σ_{Θ} of p' and Θ vs. the initial momentum p , for aluminum layer of thickness d , $0.1 \leq d \leq 8$ mm.

Tables 2, 3, and 4. The quality of the fit is described with the value of the mean squared deviation

$$\delta = \left(K^{-1} \sum_{k=1}^K (V_k / F(p_k, d_k) - 1)^2 \right)^{1/2}, \quad (2.7)$$

where the summation is over all $K \sim 400$ pairs of values of the parameters (p and d in this case) for which the values V_k have been calculated with the FLUKA code; $F(p_k, d_k)$ denotes the value of the fitting function.

3. Stopping negative muons in gaseous hydrogen

In this section we use the FLUKA code to simulate the propagation of negative muons in pure hydrogen target. In each run monochromatic collinear bunches of $N = 10^5$ muons with initial momentum p , $1 \leq p \leq 60$ MeV/c are launched in the gas with pressure H , $5 \leq H \leq 40$ Atm, the cylindric coordinates z_i and r_i of the end points T_i , $i = 1, \dots, N$ of the muon trajectories (where the muons are stopped and supposedly immediately captured in a muonic hydrogen atom, see Figure 1) are registered, and on this basis the empirical density of the spatial distribution of the muon stop points, $s(z, r; p, H)$ is evaluated as function of the initial momentum p and the hydrogen gas pressure H (assuming axial symmetry). Figure 5a is the scatter plot of the set of stopping points for a muon bunch with initial momentum $p = 30$ MeV/c, propagating in pure hydrogen at $H = 40$ Atm along the z -axis. Most of the muons are stopped at about 19 cm from the entry point, with a spread of about ± 1 cm in both longitudinal and transversal directions. Figure 5b presents the longitudinal density $S(z; p, H) = \int s(z, r; p, H) r dr$. As in Section 2, we next evaluated and tabulated the mean

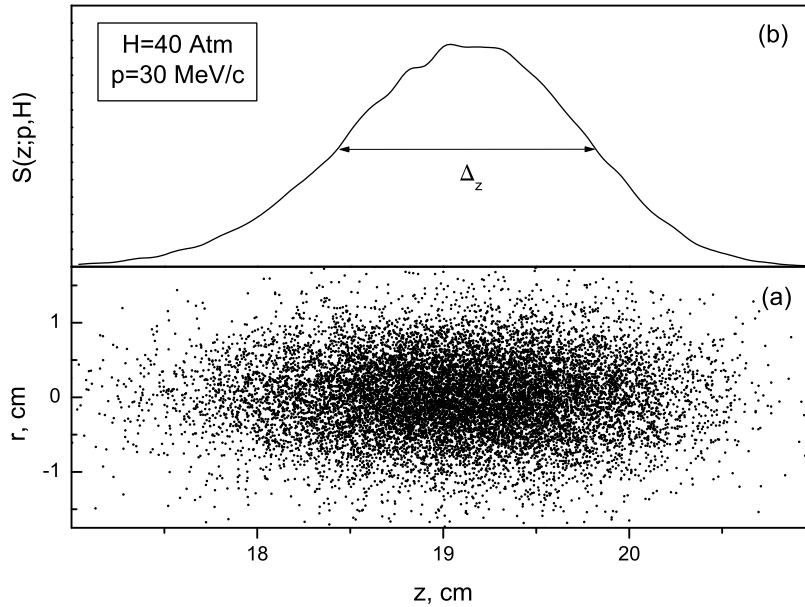


Figure 5. (a) Spatial distribution of the muon stopping positions for a collinear beam with initial momentum $p = 30$ MeV/c in pure hydrogen at pressure 40 Atm and temperature 300K. (b) Longitudinal density $S(z; p, H)$, in arbitrary units. Δ_z denotes the FWHM size of the stopping area.

values and the r.m.s. deviations of z and r as functions of the initial momentum p and the hydrogen pressure H :

$$\langle z \rangle(p, H) = \iint z s(z, r; p, H) dz r dr \quad (3.1)$$

$$\sigma_z(p, H) = \left(\iint (z - \langle z \rangle(p, H))^2 s(z, r; p, H) dz r dr \right)^{1/2} \quad (3.2)$$

(and similar for $\langle r \rangle(p, H)$ and $\sigma_r(p, H)$). Figure 6 illustrates the dependence of these quantities on the initial muon momentum p for hydrogen pressures $H = 10(10)40$ Atm. The functional

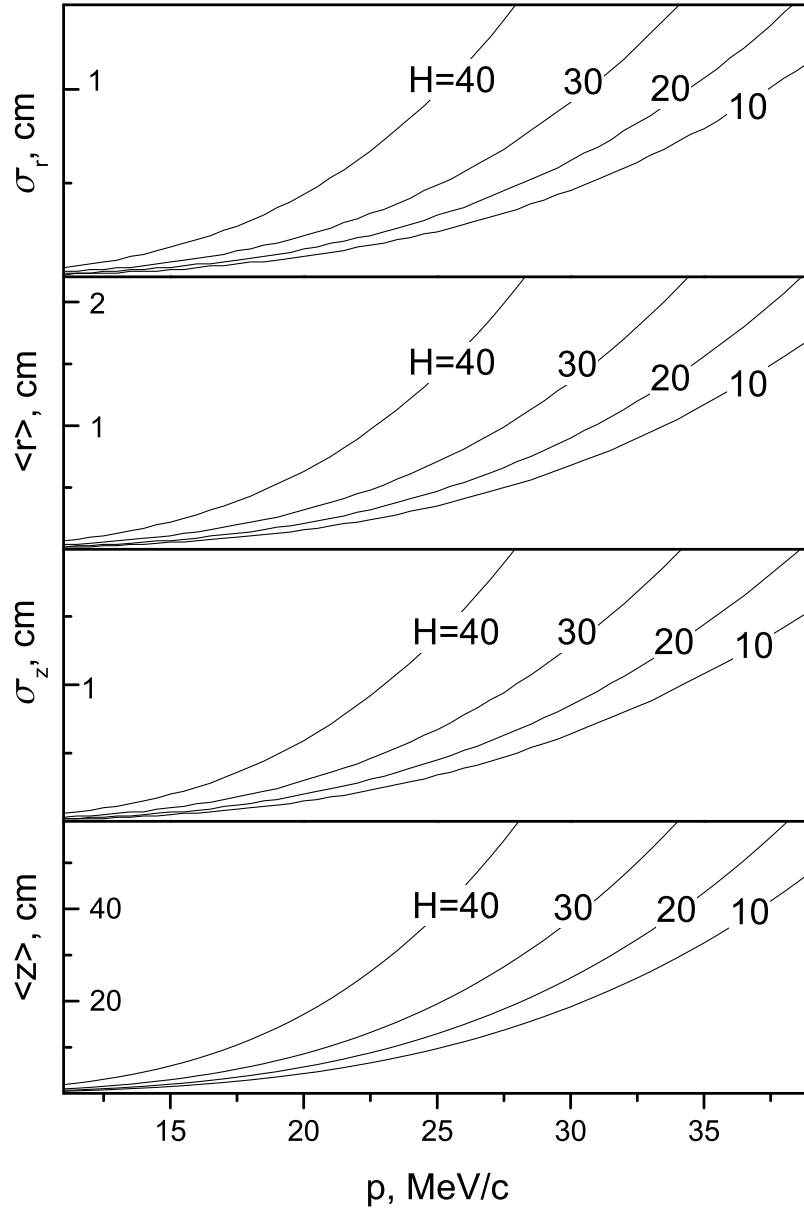


Figure 6. Muon stopping in pure hydrogen. Dependence of the mean longitudinal and transversal $\langle z \rangle(p, H)$, $\langle r \rangle(p, H)$ and their r.m.s. deviations $\sigma_z(p, H)$, $\sigma_r(p, H)$ vs. the initial momentum p , for hydrogen pressure $H = 10(10)40$ Atm.

dependence is fitted with expressions of the form:

$$b_1^{(k)}/H p^{b_2^{(k)}} \left(1 + b_3^{(k)} p^2 \exp(-b_4^{(k)} p) \right), k = 1, \dots, 4, \quad (3.3)$$

where the index $k = 1, 2, 3, 4$ labels the coefficients of the fit of $\langle z \rangle(p, H)$, $\sigma_z(p, H)$, $\langle r \rangle(p, H)$, and $\sigma_r(p, H)$, respectively. The numerical values of $b_i^{(k)}$ are given in Table 5.

4. Discussion of the results

We start by stressing once again that the results presented here are not aimed at substituting any full scale Monte Carlo simulations but only at helping the early stage design of the set-up in experiments with light gas muonic atoms.

Knowing the details of the different types of processes has proven to be useful in restricting the range of various parameters that are subject to optimization, and significantly enhances the efficiency of the full scale simulations. As an example, consider the distribution of the muon stopping points along the axis z . Figure 5(b) shows the shape of the distribution density $S(z; p, H)$ under the assumption that all muons enter the gas target with the same momentum p . In fact, after crossing the wall of the gas container the incident muon beam is no longer monochromatic and collinear; the distribution density in this case becomes

$$\tilde{S}(z; p, H) \equiv \tilde{S}(z; p, H, d, \mathbf{M}) = \int f(p'; p, d, \mathbf{M}) S(z; p', H) dp', \quad (4.1)$$

where $f(p'; p, d, \mathbf{M})$ is the final momentum distribution density for muons, launched with initial momentum p against a layer of \mathbf{M} with thickness d mm. We approximated it with the normal distribution density

$$f(p'; p, d, \mathbf{M}) \simeq N(\langle p' \rangle(p, d, \mathbf{M}), \sigma_{p'}(p, d, \mathbf{M})) \quad (4.2)$$

and similar for $s(z; p, H)$, performed numerically the integration in (4.1) and evaluated the FWHH longitudinal spread of the muon stopping area $\Delta_z(p, d, H, \mathbf{M})$. Figure 7 displays the dependence of $\Delta_z(p, d, H, \mathbf{M})$ on the initial momentum p for aluminum plates with thickness 2(1)5 mm and a 1 mm steel plate. The curves have distinct minima for which the muons stopping area is most compact as needed to satisfy Cond. 2, discussed in the Introduction. For realistic muon beams with finite initial momentum and angular spread the shape of the curves may of course be different, depending on the specific characteristic of the muon source. In any case, the full scale MC search of the optimal initial momentum may be facilitated and restricted to a narrower range by a preliminary analysis based on the results presented here.

The expressions $\langle p' \rangle(p, d, \mathbf{M})$ for the mean final momentum approximately satisfy the following scaling relations:

$$\langle p' \rangle(p, k_{\mathbf{M}} d, \mathbf{M}) \approx \langle p' \rangle(p, k_{\mathbf{M}'} d, \mathbf{M}'), \quad (4.3)$$

valid for values of p above the breakdown momentum p_0 by 5-10 MeV/c and higher (see Figure 8). We empirically determined the following values of the material-dependent coefficients $k_{\mathbf{M}}$: $k_{\mathbf{A}} = 1$, $k_{\mathbf{P}} = 2.031$, $k_{\mathbf{S}} = 0.3851$, and $k_{\mathbf{G}} = 0.2138$. The mean values of the angle of deviation $\langle \Theta \rangle(p, d, \mathbf{M})$, however, are not scaled even approximately. Knowing the angular profile of the muon beam after crossing the entrance window of the hydrogen gas target is of importance for reducing the losses

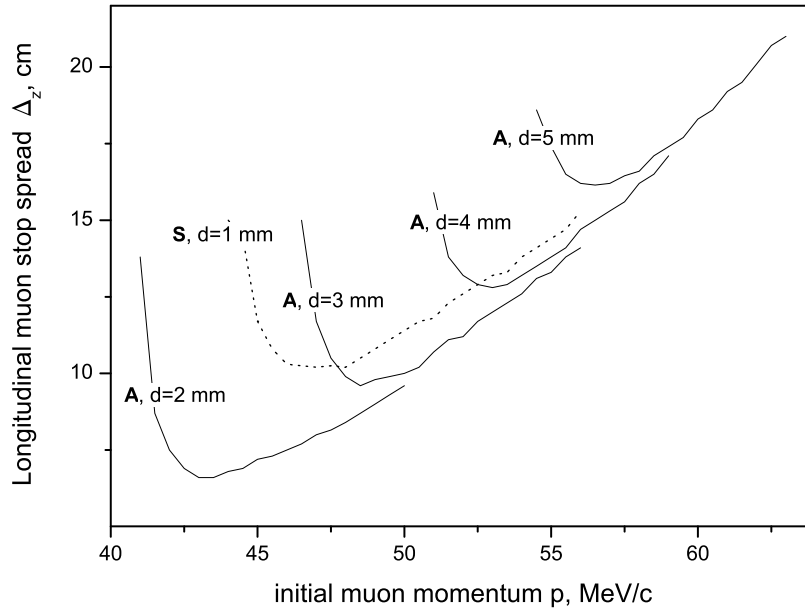


Figure 7. FWHH longitudinal size of the muon stopping area in pure hydrogen at 40 Atm and 300 K for a monochromatic collinear muon beam that has crossed aluminum plates of thickness 2(1)5 mm or a steel plate of thickness 1 mm.

of muons in the side walls. Note that the angle of deviation in hydrogen – of the order of 2° – is much smaller and can be neglected compared to the deviation angle in solid material layers.

In conclusion we add a short note about the accuracy of the various fits in Eqs. (2.3-2.6) and 3.3. Each run of the FLUKA code used a sample of 10^5 muons, so that the statistical uncertainty of the various characteristics calculated under the specific conditions of the run may assumed not to exceed 0.4%. The root mean square error δ of the fits, given in the last columns of Tables 2-5, is significantly larger, so that the statistical uncertainty can be neglected with respect to δ . The numerical uncertainty of the fitting expression coefficients is below 10^{-4} ; we checked that typing them with more than 4 digits would be in excess of the overall precision.

Acknowledgments

The authors are grateful to Dr. G. Battistoni for his help on FLUKA topics. A.A. and D.B. acknowledge the partial support from the bilateral agreement of the Bulgarian Academy of sciences and the Polish Academy of Sciences.

References

- [1] L. Essen, R.W. Donaldson, M.J. Bangham, and E.G. Hope, *Frequency of the Hydrogen Maser*, Nature **229** (1971) 110.

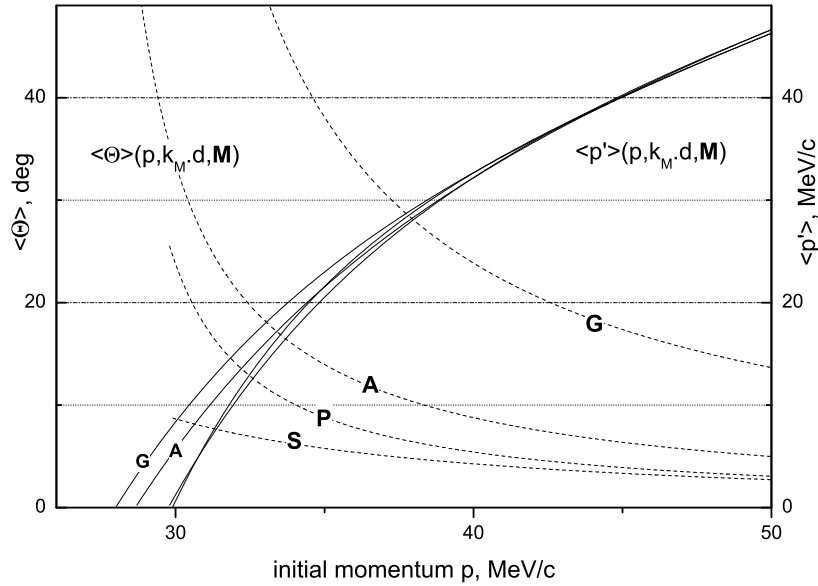


Figure 8. The plots of the mean final momentum $\langle p' \rangle$ of muon beams that have crossed a 1 mm layer of aluminum **A** or a layer of other materials **P**, **S**, **G** with thickness, rescaled according to (4.3) (the solid lines) approximately coincide for $p \geq 38$. On the contrary, the mean deviation angles $\langle \Theta \rangle$ (the dashed lines) are very different and not directly correlated with the material density.

- [2] D. Bakalov, E. Milotti, C. Rizzo, A. Vacchi, and E. Zavattini, *Experimental method to measure the hyperfine splitting of muonic hydrogen ($\mu^- p$)*. Phys. Lett. **A172**, (1992) 277.
- [3] A. Adamczak, D. Bakalov, K. Bakalova, E. Polacco, and C. Rizzo, *On the use of a $H_2 - O_2$ mixture gas target in muonic hydrogen atom hyperfine splitting experiments*, Hyperfine Interact. **136** (2001) 1.
- [4] R. Pohl, A. Antognini, F. Nez, F. Amaro, and F. Biraben, *The size of the proton*, Nature 466 (2010) 213.
- [5] A.C. Zemach, *Proton Structure and the Hyperfine Shift in Hydrogen*, Phys. Rev. 104, 1771 (1956).
- [6] A. Dupays, B. Beswick, C. Rizzo, and D. Bakalov, *Proton Zemach radius from measurements of the hyperfine splitting of hydrogen and muonic hydrogen*, Phys. Rev. **A 68** (2003) 052503.
- [7] <https://webint.ts.infn.it/en/research/exp/famu.html>
- [8] A. Adamczak, D. Bakalov, L. Stoychev, and A. Vacchi, *Hyperfine spectroscopy of muonic hydrogen and the PSI Lamb shift experiment*, Nucl. Instrum. Meth. **B 281** (2012) 72.
- [9] D. Bakalov, A. Adamczak, M. Stoilov, and A. Vacchi, *Theoretical and computational study of the energy dependence of the muon transfer rate from hydrogen to higher-Z gases*, Phys. Lett. **A 379** (2015) 151.
- [10] Masaharu Sato, Katsuhiko Ishida, Masahiko Iwasaki, Sohtaro Kanda, Yue Ma, *et al.*. *Laser spectroscopy of the hyperfine splitting energy in the ground state of muonic hydrogen*, in proceedings of 20th International Conference on Particles and Nuclei (PANIC 14), 24-29 Aug 2014, Hamburg, Germany, p.460-463. DOI: 10.3204/DESY-PROC-2014-04; ISBN: 9783935702911.

- [11] A. Werthmueller, A. Adamczak, R. Jacot-Guillarmod, *et al.*, *Energy dependence of the charge exchange reaction from muonic hydrogen to oxygen*, *Hyperfine Interact.* **116** (1998) 1.
- [12] A. Dupays, B. Lepetit, J. A. Beswick, C. Rizzo and D. Bakalov, *Nonzero total-angular-momentum three-body dynamics using hyperspherical elliptic coordinates: Application to muon transfer from muonic hydrogen to atomic oxygen and neon*, *Phys. Rev. A* **69**, 062501 (2004).
- [13] Anh-Thu Le, C.D. Lin, *Muon transfer from muonic hydrogen to atomic oxygen and nitrogen*, *Phys. Rev. A* **71** (2005) 022507.
- [14] T. Matsuzaki, K. Ishida, K. Nagamine, I. Watanabe, G.H. Eaton, W.G. Williams, *Nucl. Instrum. Meth.* **A 465** (2001) 365-383; http://www.riken.jp/en/research/labs/rnc/ral_office/
- [15] A. Ferrari, P.R. Sala, A. Fasso, and J. Ranft, *FLUKA: a multi-particle transport code*, CERN 2005-10 (2005), INFN/TC_05/11, SLAC-R-773.
- [16] T.T. Böhlen, F. Cerutti, M.P.W. Chin, *et al.*, *The FLUKA Code: Developments and Challenges for High Energy and Medical Applications*, *Nuclear Data Sheets* **120**, 211-214 (2014).
- [17] For the chemical composition of this grade of stainless steel see, e.g.,
<http://www.matdat.com/>;
http://www.finetubes.co.uk/uploads/docs/Alloy_316LN.pdf.

Table 2. Coefficients $c^{(1)}_i, i = 1, \dots, 8$ in the fit of Eq. (2.3).

M	$c_1^{(1)}$	$c_2^{(1)}$	$c_3^{(1)}$	$c_4^{(1)}$	$c_5^{(1)}$	$c_6^{(1)}$	$c_7^{(1)}$	$c_8^{(1)}$	$\delta, \%$
P	0.007726	0.002214	-0.02458	-0.02441	-0.2983	-0.2846	0.1498	-0.0006007	2.0
A	0.02084	0.004000	-0.03334	-0.2241	-1.521	-0.7395	0.1256	-0.0007018	2.1
S	0.3856	0.02971	-0.09719	-3.260	-7.605	-1.585	0.1235	-0.001216	1.1
G	1.988	0.06805	-0.1431	-4.077	-27.45	-1.579	0.08990	0.0002711	0.7

Table 3. Coefficients $c^{(2)}_i, i = 1, \dots, 6$ in the fit of Eq. (2.4).

M	$c_1^{(1)}$	$c_2^{(1)}$	$c_3^{(1)}$	$c_4^{(1)}$	$c_5^{(1)}$	$c_6^{(1)}$	$\delta, \%$
P	0.1523	0.6329	1.470	-2.521	29.25	0.27	3.9
A	0.2317	0.6877	2.370	0.2504	32.37	0.30	4.9
S	0.3450	1.094	5.125	-1.003	43.90	0.30	3.1
G	0.3478	0.3173	16.88	1.538	49.76	0.33	3.8

Table 4. Coefficients $c_{ij}^{(k)}$ and $\bar{c}_i^{(k)}, i = 1, 2, 3, k = 3, 4$ in the fit of Eqs. (2.5,2.6).

	P (Polystyrene)		A (Aluminum)		S (Stainless steel)		G (Gold)	
	$\langle \Theta \rangle, k = 3$	$\sigma_\Theta, k = 4$	$\langle \Theta \rangle, k = 3$	$\sigma_\Theta, k = 4$	$\langle \Theta \rangle, k = 3$	$\sigma_\Theta, k = 4$	$\langle \Theta \rangle, k = 3$	$\sigma_\Theta, k = 4$
$c_{00}^{(k)}$	-8.338	-4.064	-5.192	-3.554	-3.687	-6.709	-1.672	-1.831
$c_{10}^{(k)}$	-13.14	-16.92	-11.68	-17.35	-11.79	-20.63	-33.77	-52.53
$c_{20}^{(k)}$	4.708	5.541	6.593	8.686	10.43	23.15	1.215[2]	1.744[2]
$c_{30}^{(k)}$	0.7978	0.8784	1.454	1.800	4.686	9.673	1.440[2]	1.875[2]
$c_{01}^{(k)}$	0.5496	0.6676	0.3276	0.4831	0.2152	0.5402	0.1541	0.3033
$c_{11}^{(k)}$	0.2941	0.3170	0.2205	0.2674	0.1939	0.1159	0.5494	0.5068
$c_{21}^{(k)}$	-0.1353	-0.1392	-0.1704	-0.1986	-0.2374	-0.4139	-3.003	-3.612
$c_{02}^{(k)}$	0.02918	0.02546	0.01543	0.01372	0.006196	0.002691	0.007021	0.005165
$c_{12}^{(k)}$	0.01349	0.01197	0.01133	0.01136	0.007371	0.009352	0.03433	0.03460
$\bar{c}_1^{(k)}$	0.152[-3]	0.133[-3]	0.432[-4]	0.317[-4]	0.165[-4]	0.156[-4]	0.343[-6]	0.292[-6]
$\bar{c}_2^{(k)}$	-0.03851	-0.03411	-0.02567	-0.02489	-0.01329	-0.01212	-0.03038	-0.02761
$\bar{c}_3^{(k)}$	-5.166	-5.978	-9.952	-12.86	-33.81	-75.27	-1.002[3]	-1.387[3]
$\delta, \%$	2.5	4.5	2.8	3.9	0.9	1.8	5.7	4.6

Table 5. Coefficients $b^{(k)}_i, i = 1, \dots, 4, k = 1, \dots, 4$ in the fit of Eqs. (3.3). Besides the overall r.m.s. deviation δ we also give the r.m.s. deviation δ^* , evaluated with Eq. (2.7) by restricting the summation to the points with $0.5 \leq \langle z \rangle \leq 100$ cm, that are of primary interest.

	$b_1^{(k)}$	$b_2^{(k)}$	$b_3^{(k)}$	$b_4^{(k)}$	$\delta, \%$	$\delta^*, \%$
$\langle z \rangle(p, H) (k = 1)$	0.01250	1.895	0.1379	0.009103	2.1	2.3
$\sigma_z(p, H) (k = 2)$	0.0004213	3.249	-0.04348	0.2325	7.8	2.9
$\langle r \rangle(p, H) (k = 3)$	0.0003259	1.792	0.2616	0.007800	9.8	0.9
$\sigma_r(p, H) (k = 4)$	0.0003813	1.798	0.1568	0.009332	7.0	2.3